Lattice melting and superconductivity in a group IV-VI compound

Liu-Cheng Chen,[1,2] Pei-Qi Chen,[3] Wei-Jian Li,[2] Qian Zhang,[4,5] Viktor V. Struzhkin,[2] Alexander F. Goncharov,[6] Zhifeng Ren,[5] and Xiao-Jia Chen[1,2,*]

[1]*School of Science, Harbin Institute of Technology, Shenzhen 518055, China*
[2]*Center for High Pressure Science and Technology Advanced Research, Shanghai 201203, China*
[3]*Department of Electrical Engineering and Computer Science, Massachusetts Institute of Technology, Cambridge, Massachusetts 02139, USA*
[4]*Department of Materials Science and Engineering, Harbin Institute of Technology, Shenzhen 518055, China*
[5]*Department of Physics and TcSUH, University of Houston, Texas 77204, USA*
[6]*Earth and Planets Laboratory, Carnegie Institution of Washington, Washington, DC 20015, USA*

(Received 24 January 2021; revised 27 May 2021; accepted 14 June 2021; published 21 June 2021)

Inspired by the rich physical properties of IV-VI compounds, we choose polycrystalline $Pb_{0.99}Cr_{0.01}Se$ to investigate its structural, vibrational, and electrical transport properties under pressure up to 50 GPa. The structural transitions from the $B1$ to $Pnma$ phase and then to the $B2$ phase in this sample are verified by the x-ray diffraction and Raman scattering measurements. The formation of the intermediate phase is suggested to be mediated by Peierls distortion, and the broad hump in the temperature-dependent resistivity in the intermediate phase gives further evidence of this phenomenon. When the material evolves into the $B2$ phase, superconductivity is observed to emerge, accompanied by suppressing the broad hump of resistivity at intermediate temperatures. Meanwhile, Hall coefficient measurements indicate that the carrier type changes during the structural transitions. These results suggest that the superconductivity in the $B2$ phase for this material is originated by "melting" the Peierls lattice distortion. By extending the present findings to other similar IV-VI semiconductors, we propose that all group IV-VI compounds could exhibit superconductivity in their $B2$ phase due to the lattice melting at high pressures.

DOI: 10.1103/PhysRevB.103.214516

I. INTRODUCTION

The IV-VI chalcogenides have been attracting tremendous interest for many years [1]. Among them, GeTe, SnTe, and lead chalcogenides (PbX, X = S, Se, Te) are the compounds with most attractive properties. Both SnTe and GeTe have long been known for their ferroelectric properties in the low-temperature distorted structure [2]. The PbX materials have many interesting applications in optoelectronics, photovoltaic devices, and especially thermoelectric fields [3–5]. Those extensive applications are inextricably linked to their unique crystal and electronic structure properties. Under normal conditions, GeTe, SnTe, and PbX take the rocksalt crystal structure, which belongs to the $Fm\bar{3}m$ space group [6,7]. All these materials possess a direct narrow band gap occurring at the high-symmetry point L of the Brillouin zone [8]. When subjected to high pressure, SnTe and PbX share a similar sequence of phase transitions, beginning with the phase transition from NaCl type ($B1$) to a lower symmetrical phase ($Pnma$) and then going from the $Pnma$ phase to a bcc ($B2$, $Pm\bar{3}m$) structure [6,9]. Conventional wisdom advocates that the intermediate $Pnma$ phase is induced by Peierls distortion [10]. In addition, various abnormal phenomena have been presented in these IV-VI compounds at high pressures, such as the unexpected changes in resistivities and thermopowers in PbX upon compression [7,11–13]. These anomalies were always believed to be associated with the structural transformations. A mode-softening behavior at the Brillouin-zone boundary was suggested to account for the first phase transition based on the theoretical calculations [14]. Although the mechanisms [6,7,9,10] for the structural evolution with pressure become clear, the exact connection between the structures and physical properties in this model system has not been established yet. It remains unclear whether the anomalies of the physical properties are caused by the structural transformation or by the electronic transition [15,16].

In an early study [11], much attention was devoted to the explanations for the anomalies in the resistivity and thermopower of PbX in the first phase transition from $B1$ to $Pnma$, for example, whether the anomalies were connected to such a structural transition [13,17] or just related to the band gap opening [18,19]. In our recent work [20], we found that the anomalies of the physical properties in the $B1$ phase are related to the pressure-induced topological phase transition (TPT). The TPT was mainly confirmed by the sharply increased electrical conductivity, the asymmetrical form of the Seebeck coefficient, the peak of the mobility, the maxima in the linewidths of the two fundamental Raman-active phonon modes, and the minima of the difference in their frequencies. Meanwhile, a large enhancement of thermoelectric performance induced by TPT in $Pb_{0.99}Cr_{0.01}Se$ was observed. After that, the material was found to enter a topological crystalline insulator state as a result of band inversion, supported

*xjchen@hit.edu.cn; xjchen@hpstar.ac.cn

by the linear magnetoresistivity in experiments and the observed surface states by band structure calculations. These effects were realized solely by the application of pressure in the $B1$ phase in a way to avoid the possible lattice disorder. A similar band inversion and associated topological insulating state were observed in group IV-VI compounds but were realized by chemical doping [21–25]. Thus, the physics related to the anomalous behavior of the $B1$ phase and the transition to the *Pnma* phase has been addressed. At higher pressures, the electrical conductivity anomalies were observed [7], and superconductivity was reported in PbTe and PbSe and other group IV-VI compounds [12,26]. Are these anomalies related to the second phase transition from *Pnma* to $B2$? It still remains unknown why superconductivity can emerge in this system upon compression. In addition, the relationship between the structural and physical properties beyond the $B1$ phase has not been established. Finding answers to all these questions is the purpose of the present study.

In this work, we choose $Pb_{0.99}Cr_{0.01}Se$ as an example to reveal the internal correlation between the structural evolution and the associated physical properties. This material has the highest thermoelectric efficiency among all of the PbSe materials reported to date [27]. High-pressure x-ray diffraction (XRD) and Raman scattering measurements are combined to study the phase evolution. The resistivity and Hall coefficient measurements are used to investigate the physical properties. A close relationship between the structural and physical properties is given. Superconductivity in the $B2$ phase is presented. The driving force for the superconductivity in the studied material is also discussed.

II. EXPERIMENTS

The high-quality sample $Pb_{0.99}Cr_{0.01}Se$ used in this experiment was prepared by melting, hand milling, and hot pressing, as detailed elsewhere [27]. For both the XRD and Raman scattering experiments, two symmetrical diamond anvil cells with 300 μm culets were used for high-pressure studies. A sample chamber with a diameter of about 150 μm was created in a steel gasket (T301). A small piece of the sample (about $30 \times 30 \times 20\ \mu m^3$) together with small ruby balls was loaded into the sample chamber. Neon was loaded into the sample chamber to serve as the pressure medium. The XRD patterns were collected at the Advanced Photon Source, GeoSoilEnviroCARS (GSECARS) sector 13. The wavelength is 0.3100 Å, and the size of the focus beam is less than 2 μm.

The obtained two-dimensional XRD patterns were integrated into one-dimensional patterns with the help of the FIT2D software [28]. The integrated intensity vs the angle 2θ patterns were analyzed based on the Rietveld method using the software of GSAS [29]. For the Raman scattering measurements, the power of the exciting laser was kept at 1 mW with a wavelength of 488 nm to avoid possible damage to the sample. The scattered light was focused on a 1800 g/mm grating and then recorded with a 1300 pixel Princeton charge-coupled device.

The high-pressure resistivity and Hall coefficient measurements were performed in Quantum Design's physical property measurement system. The pressure was applied in a nonmagnetic diamond anvil cell made from Cu-Be alloy [30]. This customized cell has two symmetrical diamond anvils with culets of about 300 μm. A steel gasket (T301) was electrically insulated using cubic boron nitride and epoxy mixture. The sample chamber with a diameter of about 150 μm was drilled and filled by the polycrystalline sample. A standard four-probe method was used for the electrical transport measurements. The resistivity was obtained by using the van der Pauw method [31].

For all the experiments mentioned above, the pressure was calibrated by using the ruby fluorescence shift [32], and the pressure was implemented around room temperature.

III. RESULTS AND DISCUSSION

A. Structural evolution with pressure

We first perform the high-pressure synchrotron XRD measurements on the powdered polycrystal $Pb_{0.99}Cr_{0.01}Se$ at room temperature. XRD patterns up to 48.5 GPa are shown in Fig. 1(a). It can be seen that all the Bragg peaks shift to larger angles with the increase of pressure, showing the shrinkage of the lattice. At low pressures, the initial $B1$ phase is found to be stable up to 5.5 GPa. After that, there are several changes in the XRD patterns, such as the number, shape, and intensity of the peaks, suggesting the emergency of a new phase. Upon compression to 11.6 GPa, the changes in the diffraction patterns are completed. This means that the second structural phase and initial phase have a narrow coexistence region. Upon further compression, the number of Bragg peaks gradually decreases, indicating the emergence of a third phase. Figure 1(b) shows the refined results at the selected pressures of 1.2, 14.5, and 46.3 GPa by using the Rietveld method. The refinements yield model parameters of $R_{wp} = 1.72\%$ and $\chi^2 = 2.04$ for the $B1$ phase, $R_{wp} = 3.96\%$ and $\chi^2 = 6.86$ for the *Pnma* phase, and $R_{wp} = 2.13\%$ and $\chi^2 = 3.15$ for the $B2$ phase. The structures of the $B1$, *Pnma*, and $B2$ phases are shown in Fig. 1(c).

Figure 2 shows the pressure-dependent lattice parameters and volumes. Below 5 GPa, this sample has a cubic NaCl-type structure [$B1$; see Fig. 1(c)]. After that, a new structure of the orthorhombic phase emerges and shows a coexistence region with the $B1$ phase between 5.5 and 8.5 GPa. The orthorhombic phase is identified as a GeS-type structure belonging to space group D_{16}^{2h} [*Pnma*; see Fig. 1(c)]. Considering the lattice parameters of $Pb_{0.99}Cr_{0.01}Se$ ($a = 5.930 \pm 0.002$ Å for $B1$ at 5.5 GPa, and $a = 11.140 \pm 0.004$ Å, $b = 4.280 \pm 0.003$ Å, $c = 4.070 \pm 0.003$ Å for *Pnma* at the same pressure), the lattice parameters of these two phases are approximately related to each other as follows: $a(Pnma) = 2a(B1)$, $b(Pnma) = (\sqrt{2}/2)a(B1)$, and $c(Pnma) = (\sqrt{2}/2)a(B1)$. In earlier studies, it was found that the *Pnma* structure of PbTe under pressure is created by an orthorhombic distortion of the $B1$ phase [10]. The doubled period of the *Pnma* lattice is suggested to be driven by a Peierls distortion of the initial $B1$ phase [9]. For the studied system $Pb_{0.99}Cr_{0.01}Se$, the period of the initial phase is doubled along the a axis for the *Pnma* phase. Therefore, the phase transition from $B1$ to *Pnma* in $Pb_{0.99}Cr_{0.01}Se$ is suggested to be also mediated by a Peierls distortion.

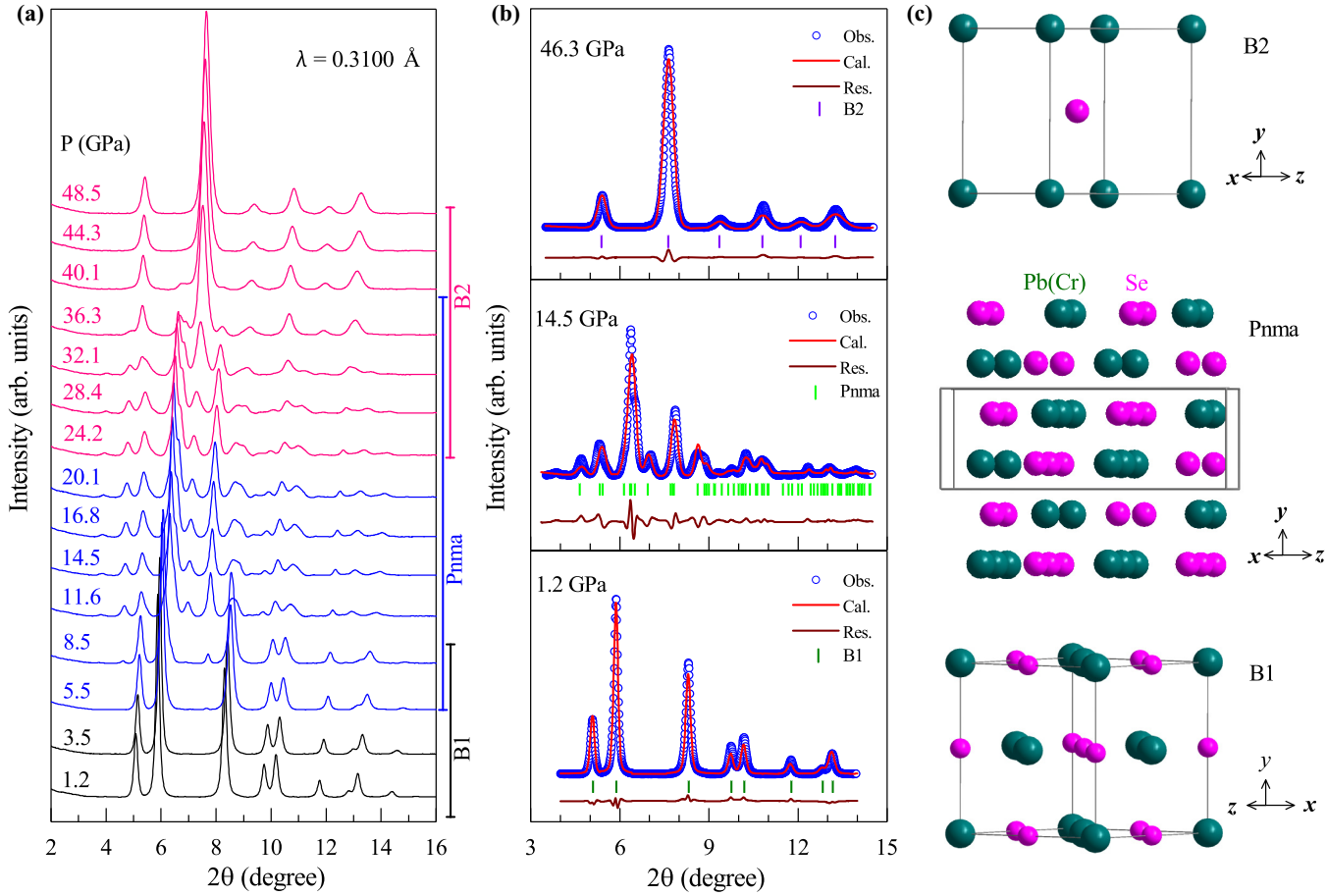

FIG. 1. (a) Synchrotron x-ray diffraction patterns of $Pb_{0.99}Cr_{0.01}Se$ at room temperature and various pressures up to 48.5 GPa. (b) Typical data points and refinement results at pressure of 1.2, 14.5, and 46.3 GPa using the Rietveld method. The experimental data points are presented as small open circles. The calculated values based on the different structures are shown by the thin curves. The Bragg peak positions are marked by the sticks in each panel. The differences between the experiments and calculations are shown by the thin curve at the bottom of each panel. (c) The structures of the $B1$, *Pnma*, and $B2$ phases, with olive circles for Pb(Cr) atoms and pink circles for Se atoms.

Upon further compression, $Pb_{0.99}Cr_{0.01}Se$ keeps the *Pnma* phase character up to 20 GPa. After that, another phase comes into sight, which is defined as a cubic CsCl-type structure [$B2$; see Fig. 1(c)]. Thus, the rapid decrease of the resistivity of PbTe after the first structural transition observed in previous studies should relate to the second structural transition [7]. At a pressure of 22 GPa, the lattice parameters are $a = 10.826 \pm 0.004$ Å, $b = 4.040 \pm 0.003$ Å, and $c = 3.880 \pm 0.003$ Å for the *Pnma* phase and $a = 3.380 \pm 0.002$ Å for the $B2$ phase. This second phase transition occurs in a wide pressure range until about 40 GPa. After that, only the $B2$ phase can be detected. The $B2$ phase is more symmetric in comparison with the *Pnma* phase. These results give a clue that the $B2$ phase is derived by the pressure-suppressed Peierls distortion in the *Pnma* phase. In Fig. 2(b), the volume evolution with pressure was fitted by using the Murnaghan equation of state [33]:

$$P = \frac{3B_0}{2}\left[\left(\frac{V}{V_0}\right)^{7/3}\right]\left\{1 + \frac{3}{4}(B_0' - 4)\left[\left(\frac{V}{V_0}\right)^{2/3} - 1\right]\right\}, \quad (1)$$

where V_0, B_0, and B_0' are the unit-cell volume, bulk modulus, and first-order derivative of the bulk modulus at ambient pressure, respectively. The fitting yields $V_0 = 57.24 \pm 0.39$ Å^3, $B_0 = 53.14 \pm 4.55$ GPa, and $B_0' = 3.2 \pm 0.2$ for the $B1$ phase; $V_0 = 52.01 \pm 0.57$ Å^3, $B_0 = 79.23 \pm 6.25$ GPa, and $B_0' = 5.6 \pm 0.6$ for the *Pnma* phase; and $V_0 = 42.90 \pm 0.44$ Å^3, $B_0 = 164.25 \pm 7.63$ GPa, and $B_0' = 4.3 \pm 0.5$ for the $B2$ phase. Here, the number of formula units per unit cell Z was induced to denote the systematic change in the volume of different phases upon compression. The Z value is 4 for both the $B1$ and *Pnma* phases and 1 for the $B2$ phase, respectively. The volume collapses from the $B1$ to *Pnma* phase and from the *Pnma* to $B2$ phase are 7.2% and 8.1%, respectively.

B. Vibrational properties under pressure

The Raman spectroscopy is an effective means for understanding the evolution of vibrational properties of materials under pressure. Generally, there is no Raman active mode in the $B1$ phase because of the symmetry constraint. However, many studies have reported the Raman active modes in the $B1$ phase of PbSe in experiments as well as in theoretical works [34,35]. As can be seen in Fig. 3(a), two phonon modes of $Pb_{0.99}Cr_{0.01}Se$ with weak and broad characters are presented at low pressures. The two phonon modes located around 40 and 135 cm^{-1} are the transverse optical (TO) and longitudinal

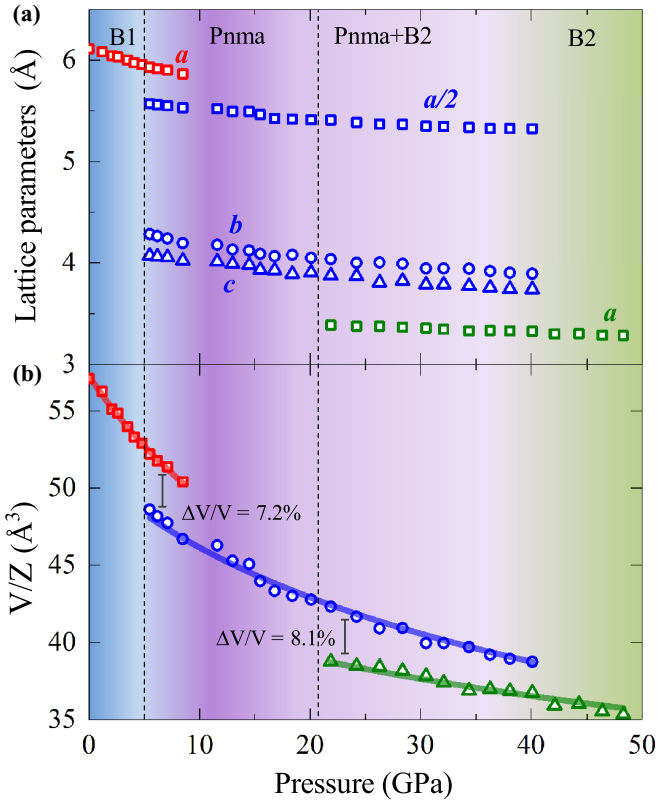

FIG. 2. (a) Pressure dependence of lattice parameters and (b) the unit-cell volumes as a function of pressure of the $B1$, *Pnma*, and $B2$ phases. The curves are the fitting results of the obtained volumes based on the Murnaghan equation of state. The dashed line represents a rough boundary between the phases.

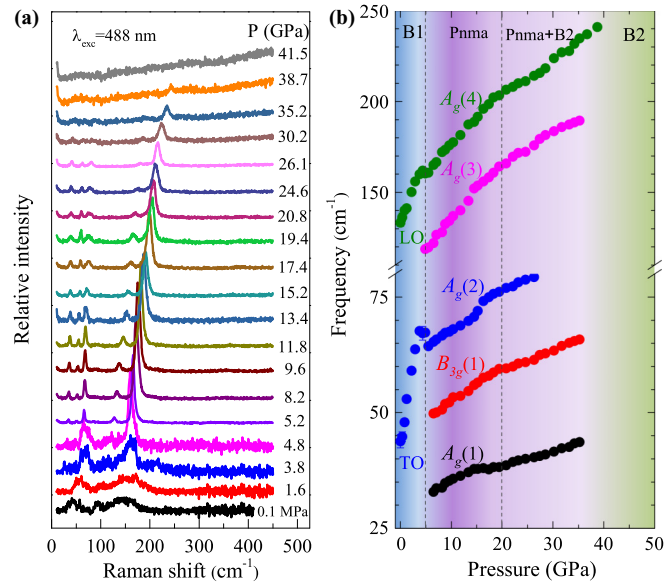

FIG. 3. (a) The selected Raman spectra of $Pb_{0.99}Cr_{0.01}Se$ at room temperature and various pressures up to 41.5 GPa. (b) The pressure dependence of the obtained phonon frequencies. The dashed line represents a rough boundary between the phases.

optical (LO) branches at the Γ point, respectively. The observed first-order Raman bands were suggested to originate from the lattice disorder [34,35]. In addition, a small peak around 90 cm^{-1} can be seen in the Raman spectra. This small peak may be the LO mode at the X point [34]. Above 5 GPa, the spectra exhibit different shapes, and many additional Raman peaks appear. This indicates a phase transition from the $B1$ to the *Pnma* phase supporting the results determined from the XRD measurements (Figs. 1 and 2). For the GeS-type structure of $Pb_{0.99}Cr_{0.01}Se$, five Raman active modes (four A_g and one B_{3g}) are detected in this study. With increasing pressure, the intensities of these Raman modes first become stronger and then are gradually suppressed. Above 38 GPa, almost all the Raman modes disappear, indicating that this sample completely transforms into the third phase ($B2$).

Using the Lorentzian-shape fitting [36] gives the extracted pressure-dependent frequencies of each phonon mode [Fig. 3(b)]. As can be seen, all the Raman modes shift toward higher frequencies under pressure. In our previous work [20], the FWHM also showed a peak at the same pressure for each mode. Both the frequency anomalies and the phonon mode width peaks are signatures of the TPT in this sample. The boundary of structural transition from the $B1$ to *Pnma* phase is clearly shown around 5 GPa. The phase transition from the *Pnma* to $B2$ phase is supported by the slope change in the pressure dependencies of the frequencies around 20 GPa. After that, the Raman modes gradually diminish upon further compression, illustrating the disappearance of the *Pnma* phase. Above 39 GPa, no detectable Raman mode is observed in the B2 phase, in agreement with XRD results (Fig. 2). Therefore, the combination of the Raman scattering and XRD measurements provides the detailed evolution paths for different phases in $Pb_{0.99}Cr_{0.01}Se$ with pressure.

C. Pressure-induced superconductivity

The charge-density wave (CDW), which is related to the Peierls lattice distortion, was generally explained by the Fermi surface nesting phenomenon [37]. The CDW distortions have been reported in thermoelectric materials [38,39], but they were predominantly observed in transition-metal dichalcogenides (TMDs) with group V metals, such as $2H$-TaS_2, $2H$-$TaSe_2$, and $2H$-$NbSe_2$, which are also known to be superconductors [40]. The interplay between the CDW order and superconductivity has been explored for a long time in condensed-matter physics. Usually, the CDW lock-in temperature T_{CDW} is higher than T_c. The application of pressure often decreases T_{CDW} and increases T_c. After the complete "melting" of the CDW phase, T_c always reaches a maximum before decreasing upon further compression. In view of the homomorphy between CDW and Peierls distortion, we expect that superconductivity in $Pb_{0.99}Cr_{0.01}Se$ can occur after the melting of the lattice distortion in the *Pnma* phase under pressure.

To verify the conjecture mentioned above, we measured the temperature dependence of the electrical transport properties for $Pb_{0.99}Cr_{0.01}Se$ under pressure. As displayed in Fig. 4(a), the resistivity has strong suppression at low pressures below 3.4 GPa and shows a metallic character as the behavior at ambient pressure [27]. The band structure calculations show that the $B1$ phase has a semiconducting character with a narrow

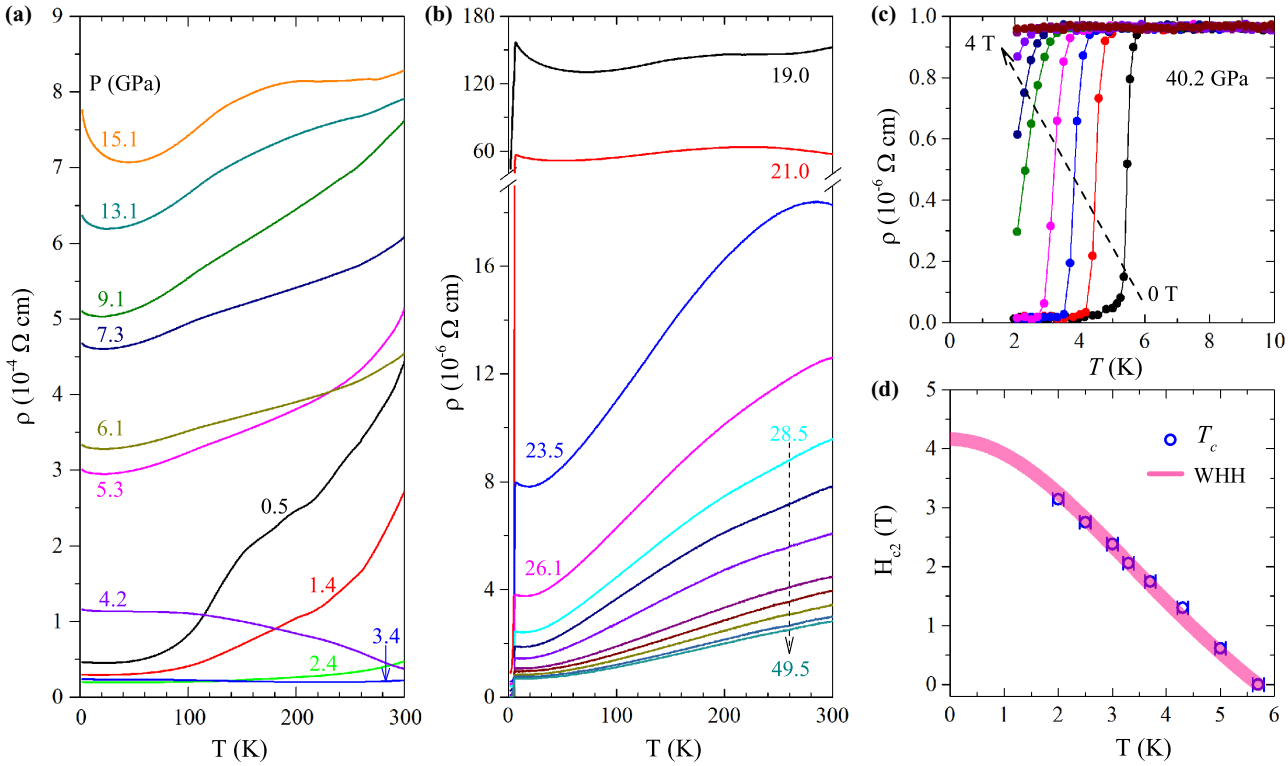

FIG. 4. (a) Temperature dependence of the resistivity of $Pb_{0.99}Cr_{0.01}Se$ at various pressures from 0.5 to 15 GPa. (b) Temperature dependence of the resistivity measured at different pressures between 19 and 50 GPa. The drop in resistivity and zero-resistivity behavior can be seen clearly. (c) Temperature dependence of the resistivity at a pressure of 40.2 GPa with the applied magnetic fields. (d) The upper critical field H_{c2} as a function of temperature at 40.2 GPa. The color area represents the calculated H_{c2} from the Werthamer-Helfand-Hohenberg (WHH) equation.

band gap at low pressures [15,20]. When pressure is increased to around 4 GPa, the resistivity has a sudden increase and has characteristic nonmetallic temperature dependence. Simultaneously, the anomalies of the pressure-dependent carrier concentration and mobility also show up [20]. These specific behaviors should relate to the change in Fermi surface as indicated by the asymmetrical form of the Seebeck coefficient [20]. These behaviors in the $B1$ phase were suggested to be caused by the pressure-driven TPT [20,41]. After that, the resistivity increases consecutively, illustrating the structural transition from the $B1$ to *Pnma* phase. Meanwhile, the resistivity behaves like a semiconductor, which is consistent with the electronic structure calculations that shown the *Pnma* structure of PbSe compound is an indirect band semiconductor [42]. Moreover, the experiments with thermoelectric power and electrical resistance give a semiconductor gap of ~0.2 eV for this compound at ~9.5 GPa [17]. Upon further compression, the resistivity has a continuous increase to 19 GPa. Obviously, this abnormal phenomenon is closely related to the structural phase transitions, as indicated by the XRD results (Figs. 1 and 2).

As shown in Fig. 4(b), the resistivity is largely suppressed by applied pressure after 19 GPa. At higher pressures, the resistivity gradually starts to behave like a metal in the normal state. This phenomenon is consistent with previous work reporting that a metal state occurs only at the high-pressure CsCl phase ($B2$) of PbSe compounds [12,17]. A pronounced resistivity drop can also clearly be seen below 6.5 K at 19 GPa, and then the resistivity drop becomes more evident with further increasing pressure. Zero resistivity at low temperatures is first observed at 37 GPa, suggesting the appearance of superconductivity in this material under pressure. To confirm the obtained superconductivity, measurements of the temperature dependence of the resistivity at various magnetic fields were performed. The results at a pressure of 40.2 GPa are summarized in Fig. 4(c). The temperature-dependent resistivity curves gradually shift towards the low temperatures with increasing magnetic fields. It seems likely that a magnetic field of about 4 T is sufficient to suppress the superconductivity at this pressure. Here, we define T_c as the onset temperature at which the drop in resistivity occurs. The upper critical field at $T = 0$ K can be given by the Werthamer-Helfand-Hohenberg equation [43]: $H_{c2}(0) = 0.693[-(dH_{c2}/dT)]_{T_c}T_c$. The calculated value of $H_{c2}(0)$ is about 4.2 T at 40.2 GPa. In Fig. 4(d), the colored areas represent the fitted temperature dependence of H_{c2} using the expression $H_{c2}(T) = H_{c2}(0)[1 - (T/T_c)^2]/[1 + (T/T_c)^2]$ based on the Ginzburg-Landau theory. The observed superconductivity in this material is consistent with previous work that showed superconductivity with $T_c \approx 6.5$ K occurs in the $B2$ phase of PbSe [12].

Thus, we find that the emergence of superconductivity in the $B2$ phase is closely followed by the disappearance of the Peierls distorted *Pnma* phase. This phenomenon is analogous to the competitive relation between CDW and superconductivity observed in TMDs [40]. The driving force of the emergence of superconductivity in $Pb_{0.99}Cr_{0.01}Se$ is closely related to the melting of Peierls lattice distortion. In

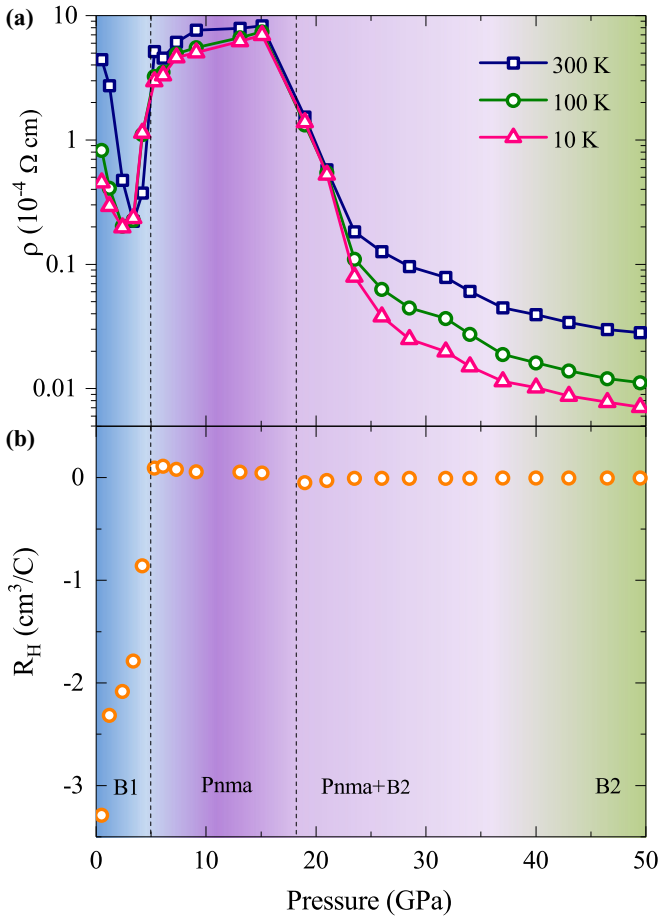

FIG. 5. (a) Pressure dependence of the resistivity at selected temperatures of 10, 100, and 300 K. (b) Pressure dependence of the Hall coefficient R_H measured at a temperature of 15 K. R_H has different signs in the different phases.

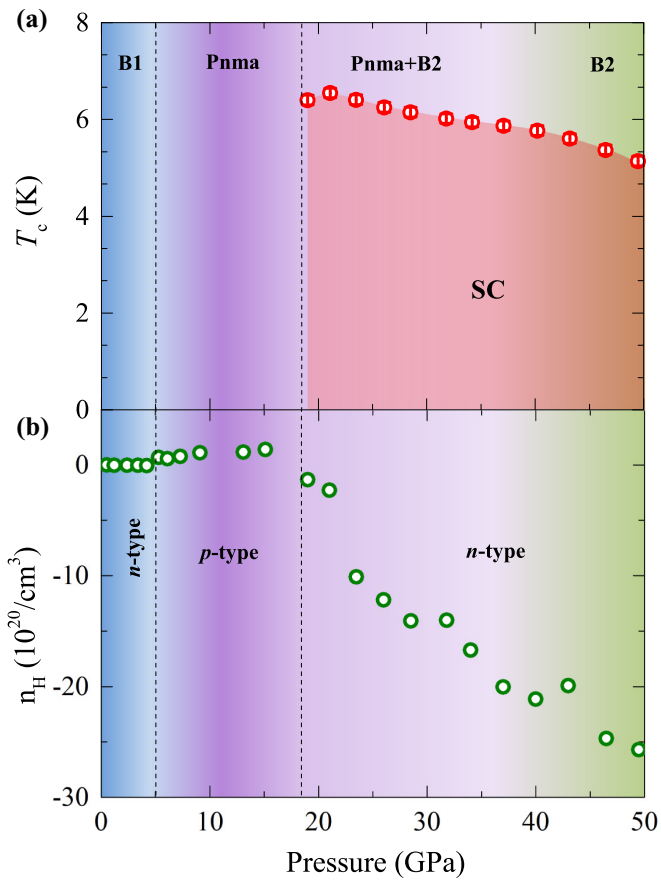

FIG. 6. (a) T_c of $Pb_{0.99}Cr_{0.01}Se$ as a function of pressure. (b) The pressure dependence of the carrier concentration n_H measured at a temperature of 15 K.

addition, it should be noticed that a broad hump centered around 180 K in the *Pnma* phase becomes more obvious with increasing pressure [Fig. 4(a)]. We argue that the broad hump should be caused by the lattice distortion in the *Pnma* phase. With the emergence of superconductivity, the broad hump becomes weaker. Then, the broad hump gradually disappears at higher pressures [Fig. 4(b)]. This behavior provides additional supportive evidence for the assertion that the melting of the lattice distortion order is the origin of the emergence of superconductivity in $Pb_{0.99}Cr_{0.01}Se$.

D. Relation between the structural and physical properties

In order to evaluate the close connection between the lattice and electronic structures and the physical properties at high pressures, we summarized the pressure dependence of the resistivity at temperatures of 10, 100, and 300 K in Fig. 5(a). It can be seen that the resistivity first decreases with pressure and then increases sharply upon further compression below 5 GPa. The emergence of the sharp valley near 3 GPa has been identified by the TPT and the occurrence of topological crystalline insulator [12,20]. When the material is driven into the *Pnma* phase, the slope of the pressure-dependent resistivity has an obvious change. This anomaly has often been observed in previous studies [7,11,12]. Now it becomes clear that this is a structural transition. After that, the resistivity has a moderate increase in the intermediate region (*Pnma*). This abnormal increase may be induced by the lattice distortion in the intermediate phase. The resistivity begins to decrease upon further compression, which is related to the second phase transition from the *Pnma* to *B*2 phase. Then, the resistivity continuously decreases with pressure.

The pressure dependence of the Hall coefficient R_H measured at 15 K is shown in Fig. 5(b). R_H is a very important parameter because it can indicate the reconstruction of the Fermi surface. As can be seen, R_H has a sharp increase with increasing pressure up to 5 GPa. At a pressure of 5 GPa, R_H displays a sign change from the negative to the positive value, giving more evidence of the phase transition from *B*1 to *Pnma*. Then R_H changes again from the positive to negative value near 19 GPa, supporting the structural transition from the *Pnma* to *B*2 phase. Therefore, the pressure-driven switching between the *n*- and *p*-type conductions reflects the changes in the electronic structure and the structural evolution in this material.

E. Pressure-temperature phase diagram

Combined with the resistivity, Raman scattering, and x-ray diffraction measurements, Fig. 6(a) gives the evolution of phase and T_c with pressure. Figure 6(b) shows the pressure

dependence of the carrier concentration n_H, which is calculated using the formula $n_H = 1/eR_H$, where e is the unit of charge. In the region of the $B1$ phase, this material shows a metallic behavior and has an n-type character. Above 5 GPa, $Pb_{0.99}Cr_{0.01}Se$ begins to enter a *Pnma* phase, accompanied by the carrier change from n type to p type. The sign change in n_H is an indication of a significant reconstruction of the Fermi surface, consistent with the occurrence of the Peierls distortion in the *Pnma* phase. When the $B2$ phase emerges and the Peierls distortion in the *Pnma* phase is largely suppressed, the sample enters a superconducting state with T_c of about 6.5 K around 19 GPa. Meanwhile, the sign of the carrier type gradually changes again from positive to negative. This indicates that the dominant electron carriers are responsible for the superconducting phase. After that, T_c shows a slow decrease with increasing pressure. Meanwhile, the absolute value of the carrier concentration has an obvious increase upon further compression, which is a positive factor for the formation of superconductivity.

For the phonon-mediated superconductivity, T_c is mostly determined by the average phonon frequency and the electron-phonon coupling constant [44]. The latter can be expressed by the combination of the electronic stiffness and the lattice stiffness [45,46]. The obtained n_H can serve as a measure of the electronic stiffness due to its tight connection with the density of states at the Fermi level. The different behaviors of T_c and n_H with pressure imply that the phonon frequency may be the key factor responsible for T_c in $Pb_{0.99}Cr_{0.01}Se$.

The results presented above together with our previous work [20] allow us to build the close relationship between the structural and physical properties for the studied material at high pressures. The high-pressure structural evolution follows the path $B1$ (NaCl type) to *Pnma* (GeS type) to $B2$ (CsCl type). In the $B1$ phase, the TPT is observed at around 3.4 GPa. This material changes from the band insulator to the topological crystalline insulator. After the structural transition from the $B1$ to *Pnma* phase, this material enters a lattice-modulated semiconducting state. Its CDW state is suppressed by the second phase transition. Meanwhile, this material evolves into a metallic state at the normal state, and superconductivity is observed at low temperatures.

IV. CONCLUSIONS

In summary, we have performed high-pressure x-ray diffraction, Raman scattering, Hall coefficient, and resistivity measurements on the polycrystalline $Pb_{0.99}Cr_{0.01}Se$ up to 50 GPa. Two phase transitions ($B1$-*Pnma*-$B2$) in this sample were clearly verified by these systematic measurements. The formation of the intermediate phase is suggested to be mediated by the Peierls distortion. The broad hump in the temperature-dependent resistivity in the intermediate phase gives further evidence of the Peierls distortion. Superconductivity was observed in the $B2$ phase, accompanied by suppression of the broad hump of resistivity at intermediate temperatures. These findings indicate that the emergence of superconductivity in the $B2$ phase is a result of pressure-induced Peierls lattice distortion. The close correlation between the structural evolution and the associated physical properties has been firmly established for this compound. The present findings can also be extended to other similar IV-VI semiconductors. Superconductivity is expected to emerge in the $B2$ phase in similar systems after melting the Peierls lattice distortion of the intermediate phase(s).

ACKNOWLEDGMENTS

The work at HIT was supported by the Shenzhen Science and Technology Program (Grant No. KQTD20200820113045081), the National Post-doctoral Program for Innovative Talents (Grant No. BX2021091), the Basic Research Program of Shenzhen (Grant No. JCYJ20200109112810241), the National Natural Science Foundation of China (Grant No. 51971081), the Cheung Kong Scholar Reward Program Young Scholar Program of China (Grant No. Q2018239), and the Natural Science Foundation for Distinguished Young Scholars of Guangdong Province of China (Grant No. 2020B1515020023). The sample preparation at the University of Houston was funded by the Department of Energy's Basic Energy Science Program (Grant No. DE-SC0010831). The work at HPSTAR was supported by the National Key R&D Program of China (Grant No. 2018YFA0305900). The work at Carnegie was funded by the U.S. National Science Foundation (Grant No. EAR-1763287). P.-Q.C. acknowledges the internship program at Carnegie Institution of Washington. The research used resources of the Advanced Photon Source, a U.S. Department of Energy (DOE) Office of Science User Facility operated for the DOE Office of Science by Argonne National Laboratory under Contract No. DE-AC02-06CH11357.

[1] *Semiconductors: Group IV Elements, IV-IV and III-IV Compounds*, Landolt-Börnstein, New Series, Group III, Vol. 41, Part A, edited by O. Madelung, U. Rössler, and M. Schulz (Springer, Berlin, 2005).

[2] M. E. Lines and A. M. Glass, *Principles and Applications of Ferroelectrics and Related Materials* (Clarendon, Oxford, 1977).

[3] S. V. Kershaw, A. S. Susha, and A. L. Rogach, Narrow bandgap colloidal metal chalcogenide quantum dots: Synthetic methods, heterostructures, assemblies, electronic and infrared optical properties, Chem. Soc. Rev. **42**, 3033 (2013).

[4] N. K. Mudugamuwa, D. M. N. M. Dissanayake, A. A. D. T. Adikaari, and S. R. P. Silva, Broadband energy harvesting with nano-composite PbS-nanocrystal/excimer laser crystallized thin film silicon hybrid solar cells, Sol. Energy Mater. Sol. Cells **93**, 549 (2009).

[5] Q. Zhang, F. Cao, W. S. Liu, K. Lukas, B. Yu, S. Chen, C. Opeil, D. Broido, G. Chen, and Z. F. Ren, Heavy doping and band engineering by potassium to improve the thermoelectric figure

of merit in *p*-type PbTe, PbSe, and $PbTe_{1-y}Se_y$, J. Am. Chem. Soc. **134**, 10031 (2012).

[6] T. Chattopadhyay, A. Werner, H. G. von Schnering, and J. Pannetier, Temperature and Pressure Induced Phase Transition in IV-VI Compounds, Rev. Phys. Appl. **19**, 807 (1984).

[7] Y. Fujii, K. Kitamura, A. Onodera, and Y. Yamada, A new high-pressure phase of PbTe above 16 GPa, Solid State Commun. **49**, 135 (1984).

[8] R. Dalven, Electronic structure of PbS, PbSe, and PbTe, Solid State Phys. **28**, 179 (1974).

[9] Y. C. Li, C. L. Lin, H. Li, X. D. Li, and J. Liu, Phase transitions in PbTe under quasi-hydrostatic pressure up to 50 GPa, High Pressure Res. **33**, 713 (2013).

[10] G. Rousse, S. Klotz, A. M. Saitta, J. Rodriguez-Carvajal, M. I. McMahon, B. Couzinet, and M. Mezouar, Structure of the intermediate phase of PbTe at high pressure, Phys. Rev. B **71**, 224116 (2005).

[11] G. A. Samara and H. G. Drickamee, Effect of pressure on the resistance of PbS and PbTe, J. Chem. Phys. **37**, 1159 (1962).

[12] N. B. Brandt, D. V. Gitsu, N. S. Popovich, V. I. Sidorov, and S. M. Chudinov, Superconductivity of the compounds PbTe and PbSe under high pressure, JETP Lett. **22**, 104 (1975).

[13] V. V. Shechennikov, S. V. Ovsyannikov, and A. Yu. Derevskov, Thermopower of lead chalcogenides at high pressures, Phys. Solid State **44**, 1845 (2002).

[14] L. Q. Xu, Y. P. Zheng, and J. C. Zheng, Thermoelectric transport properties of PbTe under pressure, Phys. Rev. B **82**, 195102 (2010).

[15] A. Svane, N. E. Christensen, M. Cardona, A. N. Chantis, M. van Schilfgaarde, and T. Kotani, Quasiparticle self-consistent *GW* calculations for PbS, PbSe, and PbTe: Band structure and pressure coefficients, Phys. Rev. B **81**, 245120 (2010).

[16] P. Barone, T. Rauch, D. D. Sante, J. Henk, I. Mertig, and S. Picozzi, Pressure-induced topological phase transitions in rock-salt chalcogenides, Phys. Rev. B **88**, 045207 (2013).

[17] S. V. Ovsyannikov, Vladimir. V. Shchennikov, A. Y. Manakov, A. Y. Likhacheva, Y. S. Ponosov, V. E. Mogilenskikh, A. P. Vokhmyanin, A. I. Ancharov, and E. P. Skipetrov, Unusual *B*1-*B*2 transition in PbSe under high pressure: Evidence for two intermediate phases; transport, structural, and optical properties, Phys. Status Solidi B **246**, 615 (2009).

[18] S. V. Ovsyannikov and V. V. Shchennikov, Pressure-tuned colossal improvement of thermoelectric efficiency of PbTe, Appl. Phys. Lett. **90**, 122103 (2007).

[19] S. V. Ovsyannikov, V. V. Shchennikov, S. Vict. Popova, and A. Yu. Derevskov, Semiconductor–metal transitions in lead chalcogenides at high pressure, Phys. Status Solidi B **235**, 521 (2003).

[20] L. C. Chen, P. Q. Chen, W. J. Li, V. V. Struzhkin, A. F. Goncharov, Q. Zhang, Z. F. Ren, and X. J. Chen, Enhancement of thermoelectric performance across the topological phase transition in dense lead selenide, Nat. Mater. **18**, 1321 (2019).

[21] J. O. Dimmock, I. Melngailis, and A. J. Strauss, Band Structure and Laser Action in $Pb_xSn_{1-x}Te$, Phys. Rev. Lett. **16**, 1193 (1966).

[22] T. H. Hsieh, H. Lin, J. Liu, W. Duan, A. Bansil, and L. Fu, Topological crystalline insulators in the SnTe material class, Nat. Commun. **3**, 982 (2012).

[23] S. Y. Xu *et al.*, Observation of a topological crystalline insulator phase and topological phase transition in $Pb_{1-x}Sn_xTe$, Nat. Commun. **3**, 1192 (2012).

[24] P. Dziawa, B. J. Kowalski, K. Dybko, R. Buczko, A. Szczerbakow, M. Szot, E. Łusakowska, T. Balasubramanian, B. M. Wojek, M. H. Berntsen, O. Tjernberg, and T. Story, Topological crystalline insulator states in $Pb_{1-x}Sn_xSe$, Nat. Mater. **11**, 1023 (2012).

[25] T. Liang, S. Kushwaha, J. Kim, Q. Gibson, J. J. Lin, N. Kioussis, R. J. Cava, and N. P. Ong, A pressure-induced topological phase with large Berry curvature in $Pb_{1-x}Sn_xTe$, Sci. Adv. **3**, e1602510 (2017).

[26] R. Matsumoto *et al.*, Pressure-induced superconductivity in tin sulfide, Phys. Rev. B **99**, 184502 (2019).

[27] Q. Zhang, E. K. Chere, K. McEnaney, M. L. Yao, F. Cao, Y. Z. Ni, S. Chen, C. Opeil, G. Chen, and Z. F. Ren, Enhancement of thermoelectric performance of *n*-type PbSe by Cr doping with optimized carrier concentration, Adv. Energy Mater. **5**, 1401977 (2015).

[28] A. P. Hammersley, S. O. Svensson, M. Hanfland, A. N. Fitch, and D. Hausermann, Two-dimensional detector software: From real detector to idealised image or two-theta scan, High Pressure Res. **14**, 235 (1996).

[29] B. H. Toby, EXPGUI, a graphical user interface for GSAS, J. Appl. Crystallogr. **34**, 210 (2001).

[30] A. G. Gavriliuk, A. A. Mironovich, and V. V. Struzhkin, Miniature diamond anvil cell for broad range of high pressure measurements, Rev. Sci. Instrum **80**, 043906 (2009).

[31] L. J. Van der Pauw, A method of measuring specific resistivity and Hall effect of discs of arbitrary shape, Philips Res. Rep. **13**, 1 (1958).

[32] H. K. Mao, P. M. Bell, J. W. Shaner, and D. J. Stembey, Specific volume measurements of Cu, Mo, Pd, and Ag and calibration of the ruby R_1 fluorescence pressure gauge from 0.06 to 1 Mbar, J. Appl. Phys. **49**, 3276 (1978).

[33] F. D. Murnaghan, The compressibility of media under extreme pressure, Proc. Natl. Acad. Sci. USA **30**, 244 (1944).

[34] A. H. Romero, M. Cardona, R. K. Kremer, R. Lauck, G. Siegle, J. Serrano, and X. C. Gonze, Experimental studies and *ab initio* calculations including spin-orbit effects, Phys. Rev. B **78**, 224302 (2008).

[35] O. Kilian, G. Allan, and L. Wirtz, Near Kohn anomalies in the phonon dispersion relations of lead chalcogenides, Phys. Rev. B **80**, 245208 (2009).

[36] R. K. Singh, S. N. Singh, B. P. Asthana, and C. M. Pathak, Deconvolution of Lorentzian Raman linewidth: Techniques of polynomial fitting and extrapolation, J. Raman Spectrosc. **25**, 423 (1994).

[37] M. D. Johannes and I. I. Mazin, Fermi surface nesting and the origin of charge density waves in metals, Phys. Rev. B **77**, 165135 (2008).

[38] M. L. Yao, W. S. Liu, X. Chen, Z. S. Ren, S. Wilson, Z. F. Ren, and C. P. Opeil, Anomalous CDW ground state in Cu_2Se: A wave-like fluctuation of *dc* I-V curve near 50 K, J. Materiomics **3**, 150 (2017).

[39] J. S. Rhyee, K. H. Lee, S. M. Lee, E. Cho, S. Kim, E. Lee, Y. S. Kwon, J. H. Shim, and G. Kotlia, Peierls distortion as a route to high thermoelectric performance in $In_4Se_{3-\delta}$ crystals, Nature (London) **459**, 965 (2009).

[40] H. K. Mao, X. J. Chen, Y. Ding, B. Li, and L. Wang, Solids, liquids, and gases under high pressure, Rev. Mod. Phys. **90**, 015007 (2018).

[41] Y. M. Blanter, M. I. Kaganov, A. V. Pantsulaya, and A. A. Varlamov, The theory of electronic topological transitions, Phys. Rep. **245**, 159 (1994).

[42] S. V. Streltsov, A. Y. Manakov, A. P. Vokhmyanin, S. V. Ovsyannikov, and V. V. Shchennikov, Crystal lattice and band structure of the intermediate high-pressure phase of PbSe, J. Phys.: Condens. Matter **21**, 385501 (2009).

[43] N. R. Werthamer, E. Helfand, and P. C. Hohenberg, Temperature and purity dependence of the superconducting critical field, H_{c2}. III. Electron spin and spin-orbit effects, Phys. Rev. **147**, 295 (1966).

[44] W. L. McMillan, Transition temperature of strongly coupled superconductors, Phys. Rev. **167**, 331 (1968).

[45] X. J. Chen, V. V. Struzhkin, S. Kung, H. K. Mao, R. J. Hemley, and A. N. Christensen, Pressure-induced phonon frequency shifts in transition-metal nitrides, Phys. Rev. B **70**, 014501 (2004).

[46] X. J. Chen, V. V. Struzhkin, Z. G. Wu, R. E Cohen, S. Kung, H. K. Mao, R. J. Hemley, and A. N. Christensen, Electronic stiffness of a superconducting niobium nitride single crystal under pressure, Phys. Rev. B **72**, 094514 (2005).